



Originally published as:

Xiong, C., Zhou, Y., Lüher, H., Ma, S.-Y. (2016): Diurnal evolution of the F region electron density local time gradient at low and middle latitudes resolved by the Swarm constellation. - *Journal of Geophysical Research*, 121, 9, pp. 9075–9089.

DOI: <http://doi.org/10.1002/2016JA023034>

## RESEARCH ARTICLE

10.1002/2016JA023034

## Key Points:

- The Ne gradient between Swarm A and C is used for the first time to investigate the *F* region electron density diurnal variations
- The Ne gradient between Swarm A and C shows prominent longitudinal wave patterns
- The phase of DE3 in  $\Delta Ne$  is found to be delayed by 6 h compared to that in Ne

## Correspondence to:

C. Xiong,  
bear@gfz-potsdam.de

## Citation:

Xiong, C., Y.-L. Zhou, H. Lühr, and S.-Y. Ma (2016), Diurnal evolution of the *F* region electron density local time gradient at low and middle latitudes resolved by the Swarm constellation, *J. Geophys. Res. Space Physics*, 121, 9075–9089, doi:10.1002/2016JA023034.

Received 8 JUN 2016

Accepted 28 AUG 2016

Accepted article online 2 SEP 2016

Published online 20 SEP 2016

## Diurnal evolution of the *F* region electron density local time gradient at low and middle latitudes resolved by the Swarm constellation

Chao Xiong<sup>1</sup>, Yun-Liang Zhou<sup>2</sup>, Hermann Lühr<sup>1</sup>, and Shu-Ying Ma<sup>2</sup>

<sup>1</sup>GFZ German Research Centre for Geosciences, Potsdam, Germany, <sup>2</sup>Department of Space Physics, College of Electronic Information, Wuhan University, Wuhan, China

**Abstract** In this study we have provided new insights into the local time gradient of *F* region electron density ( $\Delta Ne$ ) derived from the lower pair of Swarm satellites flying side by side. Our result shows that the electron density (*Ne*) increase starts just at sunrise, around 06:00 LT, simultaneously at low and middle latitudes due to the increased photoionization. At equatorial latitudes the increase in electron density gets even steeper after 07:00 LT, and the steepest increase of electron density (about  $3 \cdot 10^{10} \text{ m}^{-3}$  within 6 min) occurs around 09:00 LT. We suggest that the upward vertical plasma drift in connection with the buildup of the equatorial fountain effect plays a major role. We also found that the local time variations of the equatorial ionization anomaly (EIA) crest electron density during daytime are similar to the respective evolutions at the equator, but about 1–2 h delayed. We relate this delay to the response time between the equatorial electric field and the buildup of the plasma fountain. At equinox months a fast decrease of the *F* region electron density is seen at the EIA trough region during the prereversal enhancement, while an increase is found meanwhile at crest regions. Afterward, a fast decrease of the EIA crest electron density occurs between 19:00 and 23:00 LT, with seasonal dependence. The local time gradient between Swarm A and C shows also prominent longitudinal wave-4 pattern around August months, and the phase of DE3 in  $\Delta Ne$  is found to be delayed by 6 h compared to that in *Ne*.

### 1. Introduction

A well-known phenomenon of the low-latitude *F* region ionosphere during daytime is the equatorial ionization anomaly (EIA), which is characterized by an electron density trough above the magnetic equator and double crests of enhanced electron density at about 15° north and south of the magnetic equator [Namba and Maeda, 1939; Appleton, 1946; Liang, 1947]. The formation of EIA is generally accepted to be driven by the equatorial fountain effect. At the equatorial region the magnetic field lines are horizontally pointing northward, and the daytime eastward electric field drives the plasma upward via  $E \times B$  drift. Due to gravitational and pressure gradient forces, the up-lifted plasma at higher altitudes eventually diffuses downward along the geomagnetic field lines into both hemispheres, forming the two density crests [Duncan, 1959].

At the equatorial ionospheric *E* region, the daytime eastward electric field is due primarily to the *E* region wind dynamo, which is driven by tidal oscillations of the thermosphere [Chapman and Lindzen, 1970; Heelis, 2004; Kelley, 2009]. The neutral wind-driven currents and the gradients in *E* region conductivity generate polarization electric fields, causing the ionospheric plasma to drift primarily in the direction of the *E* region neutral wind. These polarization electric fields at low-latitude ionosphere mainly show an eastward zonal component during daytime [Eccles *et al.*, 2015]. The eastward electric field is also the driving force for the equatorial electrojet (EEJ) and the vertical plasma drift. There have been earlier studies focusing on the relation between the EEJ or electric field and the daytime electron density distributions at low latitudes. Abdu *et al.* [1990] compared the EEJ strength at Brazilian longitudes with the height of *F*<sub>2</sub>-layer peak, and they found a positive correlation between the two parameters depending on local time. Huang *et al.* [1989] found a day-to-day variation of the correlations between EEJ and the EIA crest magnitude and latitude based on the total electron content (TEC) observations at low latitudes. By comparing ground-based EEJ and eastward electric field measurements with the in situ electron density of CHAMP satellite, Stolle *et al.* [2008] found a typical response time of the EIA to variations of the EEJ and the eastward electric field of about 2–4 h and 1–2 h, respectively; they suggested that the response time is also dependent on the height of populated flux tube and the intensity of meridional wind.

The local time variation of EIA has been obtained by observations from both ground-based instruments and in situ measurements. With a low-latitude ionospheric tomography network, *Yeh et al.* [2001] found that the EIA crests typically appear at about 09:00 LT and move poleward with a speed of about  $1^\circ$  in latitude per hour for the next 2 h. *Liu et al.* [2007] reported that the crest-to-trough ratio (CTR) of EIA observed by the CHAMP satellite gradually increased from morning to noon hours and reached the maximum value between 18:00 and 19:00 LT. By using nearly 10 years data from both the CHAMP and Gravity Recovery and Climate Experiment satellites, *Xiong et al.* [2013] found that the electron density and the magnetic latitudes of the EIA crests both peaked around 14:00 LT, while the CTR peaked around 20:00 LT, with a value almost twice the daytime level. The rapidly increasing CTR value after sunset hours is primarily related to the prereversal enhancement (PRE), which is defined as a sharp increase in the plasma vertical drift after sunset via an enhancement of the eastward electric field in the ionospheric  $F$  region. The mechanism responsible for PRE is still under investigation, and the  $F$  region dynamo, driven by  $F$  region wind caused by the absorption of energy in the upper atmosphere, is generally accepted for causing the PRE [Kelley, 2009]. During daytime the  $E$  region conductance is larger than the integrated  $F$  region conductance. Therefore, the  $F$  region electric fields are dominated by the  $E$  region dynamo. However, after sunset the  $E$  region conductance decays quickly, while the  $F$  region decays slowly persisting through the night. The  $F$  region neutral wind dynamo can generate large vertical electric fields during night [Rishbeth, 1971a, 1971b; Eccles et al., 2015].

With more and more low-Earth-orbiting satellites, some other features related to EIA, such as the interhemispheric asymmetry during solstice seasons and the longitudinal wave patterns, have been widely reported. The interhemispheric asymmetry of EIA was mainly attributed to the asymmetric neutral composition and the summer-to-winter (transequatorial) neutral wind effects [Aydogdu, 1988; Lin et al., 2007; Ram et al., 2009], while the longitudinal wave patterns of the EIA were mainly attributed to the various tidal forces from the lower atmosphere [e.g., Sagawa et al., 2005; Immel et al., 2006; Lühr et al., 2012; Xiong and Lühr, 2013]. Most of these studies were focusing on the daytime ionosphere when the EIA is well developed, while in this paper we aim to provide some details of the  $F$  region electron density local time gradient derived from the lower pair of Swarm constellation. The two spacecraft, Swarm A and C, flying side by side with longitudinal separation of  $1.4^\circ$ , corresponding to about 6 min difference in local time, are suitable for such a purpose. The identical instrumentation on board the Swarm spacecraft makes our obtained results more reliable.

In the section to follow we first introduce the data set. In section 3 we present the diurnal variations of  $F$  region electron density local time gradient derived from Swarm A and C. For comparison, the local time gradient derived from single spacecraft, Swarm A, has also been presented. In the discussion part we compare the Swarm observations with vertical plasma drift measurements from the Jicamarca radar and provide the relevant interpretations. Finally, we summarize the main findings from our results.

## 2. Instruments and Data Set

### 2.1. Swarm Constellation

The Swarm mission, comprising three spacecraft, was launched on 22 November 2013 into a near-polar ( $87.5^\circ$  inclination) orbit with initial altitude of about 500 km. From January 2014 onward the three spacecraft were maneuvered apart and achieved their final constellation on 17 April 2014. From then on the lower pair, Swarm A and C, is flying side by side at an altitude of about 470 km, with a longitudinal separation of about  $1.4^\circ$ . The third spacecraft, Swarm B, orbits the Earth at about 520 km with a somewhat higher inclination. The plasma density data set measured by the Electric Field Instrument onboard Swarm is available at <http://earth.esa.int/swarm>. In this study we are using the Langmuir Probe-derived plasma density data with a time resolution of 2 Hz.

### 2.2. Incoherent Scatter Radar at Jicamarca

The vertical plasma drift data we used are measured by the incoherent scatter radar (ISR) at Jicamarca ( $11.95^\circ\text{S}$ ,  $76.87^\circ\text{W}$ ), which has been in operation since the 1960s. The primary operation mode of the Jicamarca ISR is the east-west drift experiment, which aims to estimate the  $E \times B$  plasma drift perpendicular to the magnetic field from a pair of measured line-of-sight drift velocities. A detailed description of the  $F$  region drift measurements by the Jicamarca radar has been given by *Kudeki et al.* [1999]. The  $E \times B$  records were obtained at 5 min cadence, covering the altitude range from 45 km to 900 km at steps of 15 km. For comparison with the Swarm

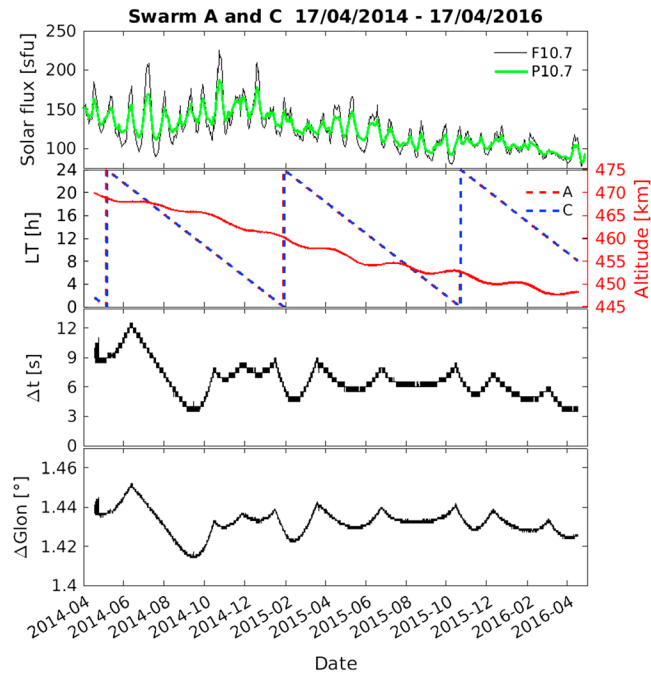


**Figure 1.** (first panel) The solar activity index  $F_{10.7}$  (black) and  $P_{10.7}$  (green) variations during the 2 year period from 17 April 2014 to 17 April 2016. (second panel) The local time evolution of the ascending node for Swarm A (red dashed) and C (blue dashed), and the red solid curve indicates the altitude of Swarm A. (third and fourth panels) The evolution of the leading time (in UT) and longitudinal separation between Swarm C and A.

electron density observations, the vertical plasma drift measurements are of more interest at altitudes around 450 km.

### 3. Observations

#### 3.1. Examples of the Electron Density Local Time Gradient Between Swarm A and C

Within this study we took the electron density measurements from Swarm A and C during 2 year period (from 17 April 2014 to 17 April 2016). As shown in Figure 1, the solar activity index,  $P_{10.7}$ , which is defined as  $P_{10.7} = (F_{10.7} + F_{10.7A})/2$ , where  $F_{10.7A}$  is the 81 day averaged value of  $F_{10.7}$ , decreased from above 175 solar flux unit (sfu) to below 100 sfu during the 2 year period. The altitude of Swarm A and C decayed from about 470 km to 450 km (indicated by the red solid curve in the second panels). Their local time evolutions of the ascending node have been indicated by the red and blue dashed lines. After the final constellation

has been completed on 17 April 2014, Swarm C flies a few seconds (in universal time, UT) ahead of Swarm A. From the third panel of Figure 1, we see that the leading time,  $\Delta t$ , between the two spacecraft varies between 3 and 12 s. With such a short leading time, we could consider that Swarm A and C simultaneously probe the  $F$  region ionosphere along their orbits. Their longitudinal separation (Swarm A is on the westside),  $\Delta \text{Glon}$ , was also quite stable, which varied between  $1.4^\circ$  and  $1.45^\circ$  during the 2 year period.

The  $1.4^\circ$  longitudinal separation between Swarm A and C corresponds to about 6 min in local time (LT) frame. To see whether the  $F$  region electron density gradient within 6 min LT can be well represented, Figure 2 shows two examples of typical electron density profiles along the magnetic latitude (MLAT) measured by the two spacecraft. Figure 2a shows one example observed around 09:50 LT, and the red and green curves indicate the  $N_e$  profiles measured by Swarm A and C, respectively. The epochs, altitudes, and longitudes when the spacecraft passed the geographic equator are listed in the topside. For this event Swarm C was flying 7 s (in UT) ahead of Swarm A. The electron density profiles probed by the two spacecraft are generally similar, both showing two crests of EIA at about  $\pm 10^\circ$  MLAT. Despite the similarity, slight difference can also be found between them. For example, the EIA crests observed by Swarm C have larger electron density and are further away from the magnetic equator, while at the EIA trough region it observed lower electron density. As Swarm A is on the westside, which is 6 min earlier in LT than Swarm C, the fountain effect is expected to be stronger for Swarm C during the development phase of EIA. Therefore, the slight difference between the two spacecraft measurements can possibly be attributed to their local time difference. Figure 2b presents another example around 18:40 LT, with Swarm C flying 8 s (in UT) ahead of Swarm A. The electron density profiles observed by the two spacecraft are also similar, showing two crests of EIA at about  $\pm 15^\circ$  MLAT, but differences are still found between them. The electron densities recorded by Swarm C at EIA trough region are slightly smaller than those from Swarm A, while they are larger at the EIA crest regions.

The two examples presented in Figure 2 imply that the 6 min difference in LT between Swarm A and C orbit is suitable for resolving the local time gradient of the  $F$  region ionosphere. However, the electron density local time gradient between the two spacecraft is an order of magnitude smaller than the background density, and

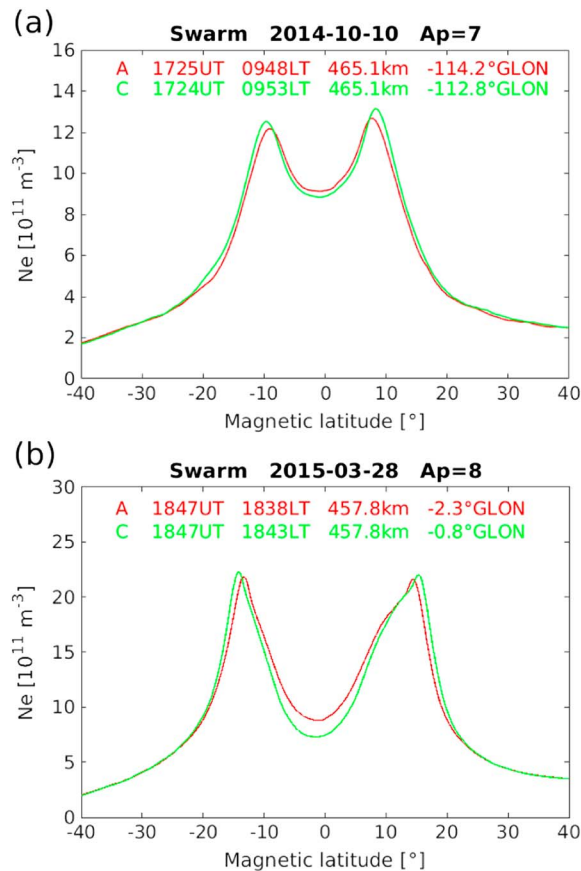


**Figure 2.** Two typical magnetic latitude profiles of electron density observed by Swarm A (red) and C (green) at low and middle latitudes around (a) 09:50 LT and (b) 18:40 LT. The epochs, altitudes, and longitudes when the spacecraft passed the geographic equator are listed in the topside.

this small difference may be affected by the instrument noise, or the small-scale structures of the  $F$  region ionosphere, such as the equatorial plasma irregularity (EPI) occurring after sunset. As found later, the Langmuir probe data of Swarm sometimes show wave-like disturbances on the electron density signals. For the example shown in Figure 3a, several packages of wave-like signals with lower amplitudes are found in the northern hemisphere from both spacecraft. The reason for the wave-like noise in the electron density data is still unknown. Figure 3b presents one example of EPI observed by Swarm A. Statistical analysis of EPIs revealed that the characteristics of EPIs observed by Swarm A and C are usually uncorrelated, although they are separated only by about 150 km in longitude [Xiong *et al.*, 2016]. In this event the plasma density depletions at the equatorial region are only observed by Swarm A, and the rapidly varying amplitudes within EPI cause large density differences between Swarm A and C, challenging our statistical analysis during the postsunset hours. Therefore, the wave-like instrument noise and EPI effects should be eliminated.

As introduced by Xiong *et al.* [2016], a multiwavelet method has been applied to the 2 Hz electron density time series for smoothing the data. The wavelet function they used is “coiflets,” which is discrete, near symmetric, and has scaling functions with vanishing moments [Beylkin *et al.*, 1991]. In this study we used the same multiwavelet method, and wavelet coefficients with wavelengths between 240 km and 960 km were used to reconstruct the background  $Ne$  profile, which are presented in Figure 3 as the black and blue dashed lines for Swarm A and C, respectively. This approach can eliminate the fast variations in the electron density profiles caused by the unknown wave-like signals as shown in Figure 3a. However, for the example presented in Figure 3b, although the small-scale depletion associated with EPI has been smoothed out, the large-scale depletion ( $>240$  km) makes the electron density curve of Swarm A (black dashed line) deviates largely from that of Swarm C (blue dashed line), and this deviation is clearly not attributed to the local time gradients. In view of this, the orbits detected with EPIs have been abandoned.

### 3.2. The Normalization of $Ne$ by Solar Activity and Intersatellite Calibration

Before the statistical analysis there are still two questions that need to be addressed. One is the altitude and solar activity dependencies of the  $F$  region ionosphere. As seen from Figure 1 the altitude of Swarm A has decayed from about 470 km to 450 km during the considered 2 year period (the same for Swarm C, not shown here). Compared to the typical value of the topside vertical scale height, which is usually larger than 100 km at low and middle latitudes [Liu *et al.*, 2008], the 20 km altitude decay of Swarm during considered 2 year period is neglected in this study. The solar activity index,  $P_{10.7}$ , reduced from about 175 sfu to below 100 sfu. The Swarm orbits precess slowly in local time, which also means that for different local times the electron density measurements correspond to different solar activity levels. Therefore, the reduced solar activity could

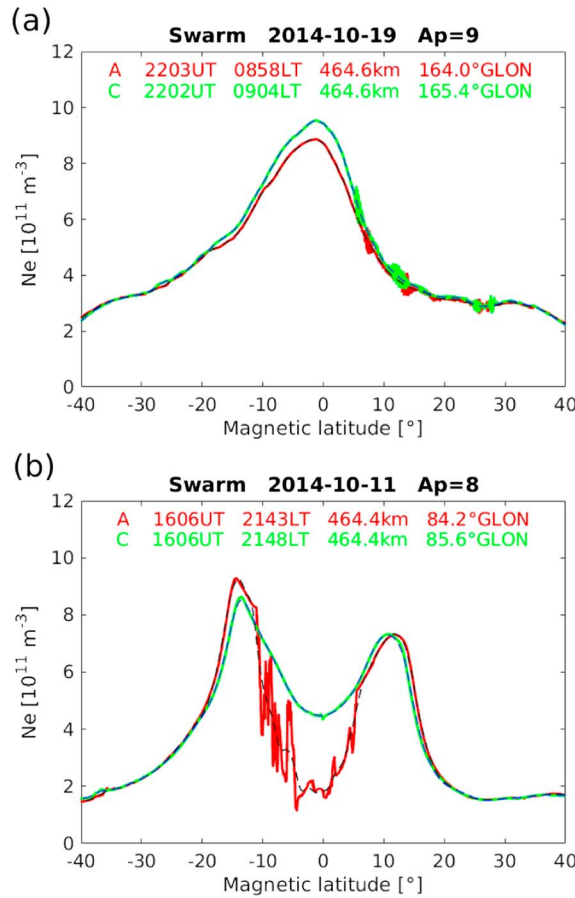


**Figure 3.** Similar as Figure 2 but with (a) wave-like noise and (b) equatorial plasma irregularity (EPI) observed by Swarm A. The black and blue dashed lines represent the electron density profiles smoothed with a multiwavelet method.

in Figure 4b, for each season, the  $Ne$  observations between  $\pm 60^\circ$  MLAT have been averaged over all longitudes, and the local time variations are almost identical between the two satellites during all three seasons, which confirm the consistence between the two instruments. Additionally, for each season we further derived a scaling factor,  $\alpha$ , between the two satellites, defined as

$$\alpha = \frac{Ne_{swa}}{Ne_{swc}} \quad (2)$$

where  $Ne_{swa}$  and  $Ne_{swc}$  are the diurnal mean value of  $Ne$  for the two satellites. The value of  $\alpha$  is derived as 1.013, 1.010, and 1.019 for the three seasons, respectively, and finally, we used the average value, 1.01, of the scaling factor between the two spacecraft for the whole data set. For deriving the electron density local time gradient between them, the normalized  $Ne$  measurements from Swarm C has first multiplied by the scaling factor,  $\alpha = 1.01$  and then subtract the  $Ne$  measurements from Swarm A. The uncertainties caused by the instrument difference between the two satellites are believed to be reduced.

For statistical analysis, the electron density data sets were further divided into the three Lloyd seasons: December solstice months (November–February), equinoxes months (March, April, September, and October), and June solstice months (May–August). Geomagnetic active days with  $Ap > 15$  were excluded to reduce geomagnetic storm-related effects.

### 3.3. The Diurnal Evolution

Before showing the electron density local time gradient between Swarm A and C, we first went back to the original electron density measurements ( $Ne$ , normalized by  $P_{10.7}$ ) and binned the data from Swarm A into

possibly add some uncertainties to our results. For normalization of  $Ne$  by solar activity, we first derived the daily averaged  $Ne$  measurements from the two spacecraft at low and middle latitudes ( $\pm 60^\circ$  MLAT). As shown in Figure 4a, the daily averaged  $Ne$  are roughly linearly dependent on the solar activity index,  $P_{10.7}$ . According to this linear dependence, we then normalized each of the measurement to a constant solar activity level at  $P_{10.7} = 130$  sfu with the equation:

$$Ne_{norm} = Ne_{meas} \cdot \frac{a \cdot 130 + b}{a \cdot x + b} \quad (1)$$

where  $Ne_{meas}$  is the electron density measured by Swarm A and C,  $a$  ( $=0.312$ ) and  $b$  ( $=-10.624$ ) are the slope and intercept of the linear dependence as shown in Figure 4a, and  $Ne_{norm}$  is the normalized electron density at the constant solar activity level ( $P_{10.7} = 130$  sfu), which is used in the rest of the study.

The other question is the instrument-difference effects between Swarm A and C. After the  $Ne$  measurements have been normalized to  $P_{10.7} = 130$  sfu, we then sorted the data set into 1 h local time bins to get their diurnal variation. As shown

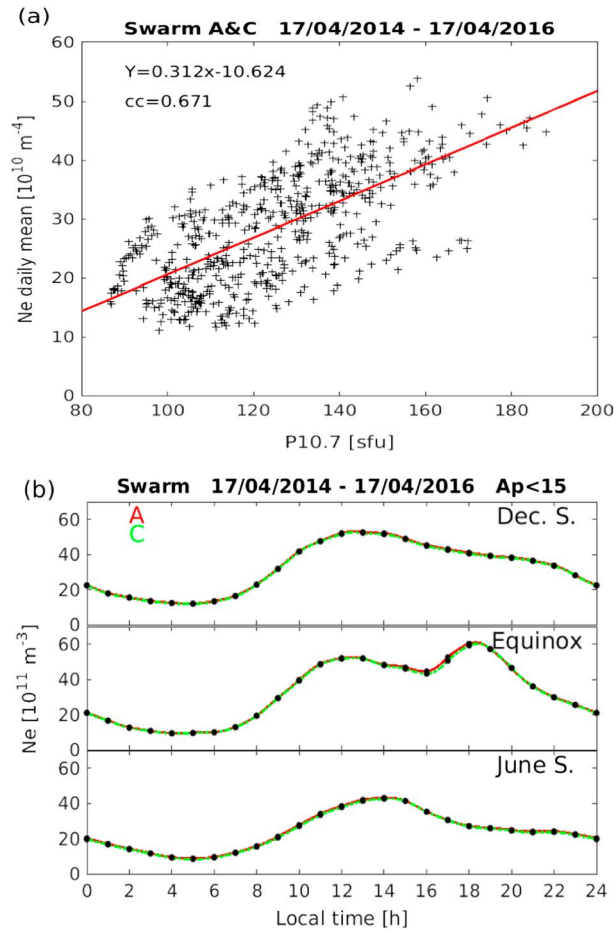


**Figure 4.** (a) The solar activity dependence of the daily mean electron density measured by Swarm A and C. (b) The diurnal variations of the electron density measured by Swarm A and C during three seasons.

MLAT (1°) and LT (0.1 h) bins for each season. As we have only 2 years data from Swarm and the magnetic active days with  $A_p > 15$  have been excluded, there are data gaps when we sort the data into 0.1 h bin. Therefore, for each latitude bin, the local time variations have been further smoothed with a 3 h boxcar for smooth out the fast variations and fill the data gap. The result from the averaged electron density of Swarm A is presented in Figure 5a. A dominant feature of the electron density at low latitudes is the equatorial ionization anomaly during daytime. A clear double crest structure of EIA appears around 10:00 LT, and the crests reach their furthest magnetic latitude (about  $\pm 15^\circ$  MLAT) around noon. Afterward, the two crests move equatorward slightly. When looked at the different seasons, the EIA two crests during daytime are more visible during December solstice and equinox seasons, while during June solstice the EIA crest at the summer hemisphere shows clearly larger electron density. The other interesting feature is that around sunset hours, the separation between the two crests increased again during equinox seasons, and the even larger electron density (compared to the values around noon) is possibly due to the unbalance data coverage of the season and local time, as we have only two years data; during December solstice the EIA crest shows larger electron density at the summer hemisphere around sunset hours, while at the same local time the EIA totally vanishes in June solstice.

For deriving the electron density local time gradient,  $\Delta Ne$ , we have used two different ways: one is from single spacecraft (e.g., Swarm A) and the other is from the difference between Swarm A and C. In Figure 5a, we have already sorted the normalized  $Ne$  measurements from Swarm A into zonal mean MLAT (1°) and LT (0.1 h) bins, and the difference between neighboring LT bins corresponds to a gradient within 6 min local time. Figure 5b presents the MLAT versus LT distribution of such gradients derived from Swarm A during three seasons. Similarly, the local time gradients have also been smoothed with a 3 h boxcar. Although the averaged  $\Delta Ne$  shows relatively small amplitudes (maximum value about  $2\text{--}3 \cdot 10^{10} \text{ m}^{-3}$ ), clear local time evolution features are seen for all seasons. The  $\Delta Ne$  is mainly positive between 06:00 and 13:00 LT, while negative for the other local times (except for 16:00–19:00 LT at equinox). This means that the  $F$  region electron density starts to increase just at sunrise, around 06:00 LT, and keeps to increase until 13:00 LT. The negative values at EIA crest regions but with smaller amplitudes (about  $1 \cdot 10^{10} \text{ m}^{-3}$ ) during afternoon hours imply that the  $F$  region electron density gradually decreases. During equinox a clear increase of electron density is found again during 16:00–19:00 LT.

For the second method, we took the normalized electron density measured by the western spacecraft, Swarm A, at earlier local time as reference and subtracted Swarm C observations from it for each pass. As Swarm A is 6 min earlier than C, the positive and negative values of  $\Delta Ne$  here mean that the  $F$  region electron density is increasing and decreasing with local time, respectively. The local time gradient ( $\Delta Ne$ ) derived

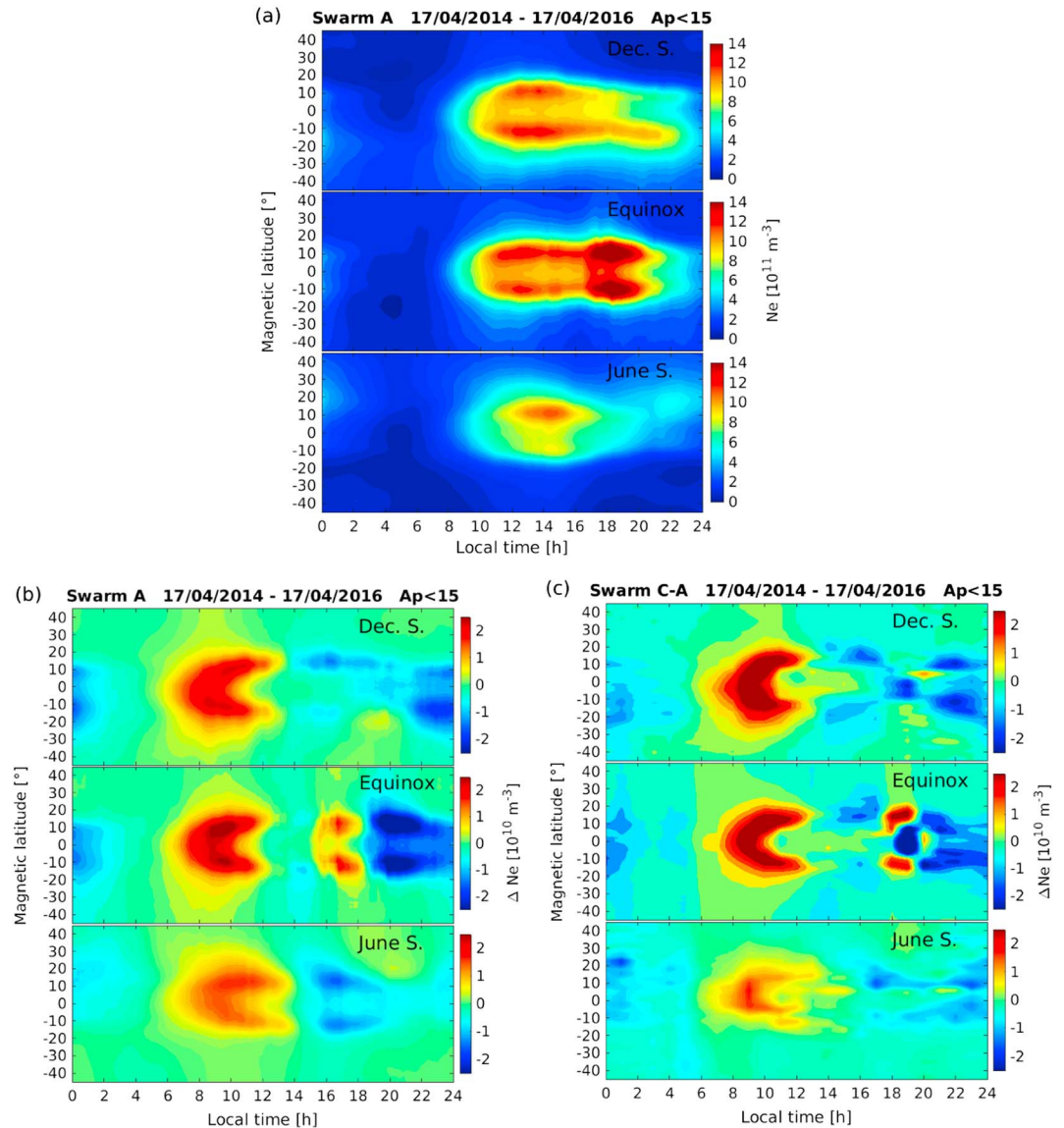


**Figure 5.** (a) Magnetic latitude and local time distribution of the average electron density observed by Swarm A separately for three seasons. (b) Similar as Figure 5a but for the electron density gradient ( $\Delta Ne$ ) derived from single satellite, Swarm A. (c) Similar as Figure 5b but for the electron density gradient ( $\Delta Ne$ ) derived from twin satellites (Swarm C minus Swarm A, the observation from the westside spacecraft at earlier local time, Swarm A, has been taken as reference). For both Figures 5b and 5c, the positive and negative values of  $\Delta Ne$  mean that the *F* region electron density is increasing and decreasing with local time, respectively.

between the two spacecraft was further sorted into zonal mean MLAT ( $1^\circ$ ) and LT (1 h) bins for each season, and the results are presented in Figure 5c. The diurnal variation of  $\Delta Ne$  derived between the two spacecraft is generally similar to that derived from single spacecraft as show in Figure 5b. However, for Figure 5c we found that between 17:00 and 19:00 LT of equinox,  $\Delta Ne$  derived between Swarm A and C shows obvious positive values at the EIA crest regions, but with negative  $\Delta Ne$  at EIA trough region, which is not seen from Figure 5b.

Figure 6 further presents the local time variations of the averaged  $\Delta Ne$  derived from both methods for three different latitude bins at the EIA trough ( $\pm 5^\circ$ ) and crest regions ( $\pm 10^\circ$  to  $\pm 20^\circ$ ). Concerning the uncertainty of the  $\Delta Ne$  derived from the difference between Swarm C and A, we obtain typical values for standard deviation,  $\sigma$ , about  $1-2 \cdot 10^{10} \text{ m}^{-3}$  for afternoon and postsunset hours, which is almost comparable to the mean value of  $\Delta Ne$ . Therefore, we have used the uncertainty of mean value in this study, which is defined as  $\sigma/\sqrt{n}$ , where  $n$  is the number of event contribution to each point. The result is presented in Figure 6b, and we see that the

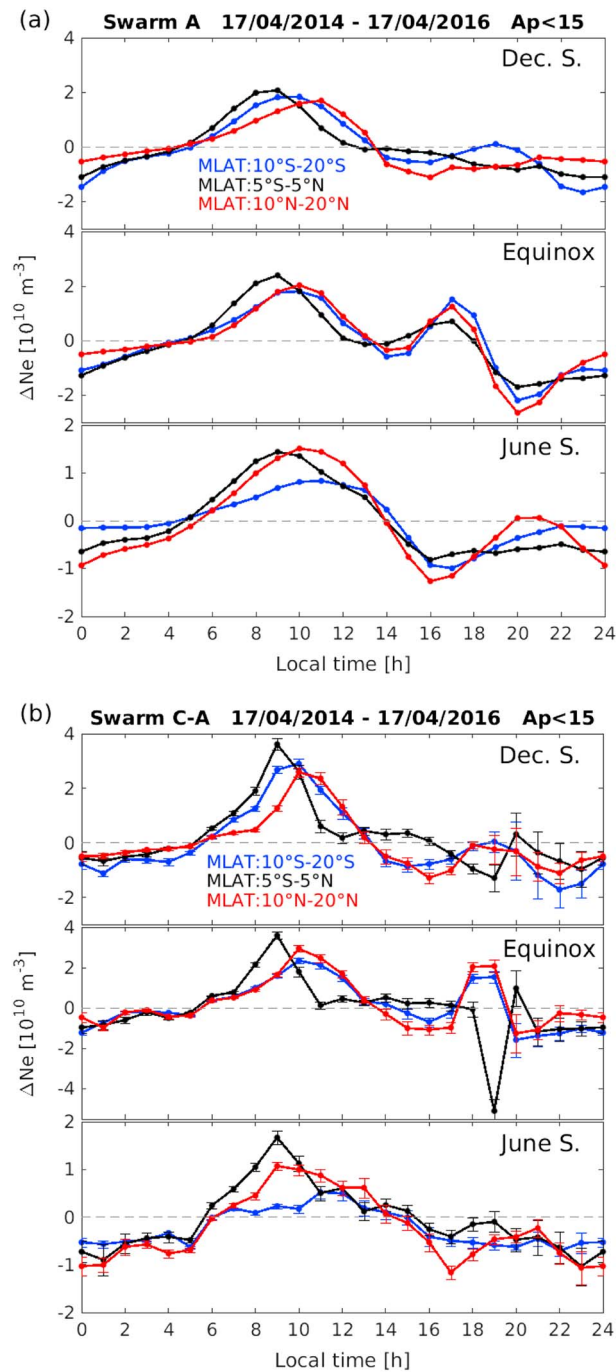


**Figure 6.** The diurnal variations of the averaged  $\Delta Ne$  derived (a) from single satellite and (b) from twin satellites at the EIA trough ( $\pm 5^\circ$ ) and crest ( $\pm 10^\circ$  to  $\pm 20^\circ$ ) regions during three different seasons. The error bar in Figure 6b indicates the uncertainty of mean value.

of local time, when only ascending or descending orbits are considered. This means that the local time gradient within 6 min derived from single spacecraft is in fact the difference between the averaged electron densities within 1.1 days. Thus, this kind of local time gradient has already been averaged over all the longitudes, and the day-to-day variability of the *F* region ionosphere may also contribute the local time gradient. By contrast, with side-by-side flying spacecraft, such as Swarm C and A, the electron densities are nearly simultaneously measured and the difference between them represents better the gradient at a certain time

diurnal evolution of  $\Delta Ne$  is statistically significant, clearly larger than the corresponding uncertainty of mean value. From both methods we see that  $\Delta Ne$  at the trough region changes sign from negative to positive shortly before 06:00 LT and reaches its maximum value at 09:00 LT during all seasons. Afterward, it starts to decrease, except during the equinox season around 16:00 LT as shown in Figure 6b. From 06:00 to 16:00 LT the evolution of  $\Delta Ne$  at crest regions is generally similar to that at the trough region, but with some time delay. For example,  $\Delta Ne$  at EIA crest regions reaches its maximum value around 10:00 LT, which is 1 h later than that at the magnetic equator. During equinox, obvious difference at 17:00–20:00 LT can be found in the electron density gradient derived from the two methods. For example, for the gradient derived from single satellite (Figure 6a), an increase with peak values at 17:00 LT is found at both EIA trough and crest regions; while for the gradient derived between the two spacecraft (Figure 6b),  $\Delta Ne$  at the trough region is seen with a negative value at 19:00 LT, which we consider to correspond to the onset time of the prereversal enhancement (PRE).

## 4. Discussion

### 4.1. The Electron Density Local Time Gradients Derived From Single or Twin Spacecraft

In principle, the similar local time variations of  $\Delta Ne$  between Figures 5b and 5c suggest that the electron density gradients derived from single and twin spacecraft reflect reliable results. However, the near-polar orbit satellites, such as Swarm A, take about 266 days for covering all 24 h

and location. From this point of view, we consider the electron density difference between Swarm A and C can better represent the local time gradient and therefore mainly discuss this kind of local time gradient in the rest of the study.

As shown in Figures 5 and 6, the different behavior of  $\Delta Ne$  around 17:00 LT during equinox months may partly be attributed to that  $\Delta Ne$  derived from single satellite representing the difference between the longitudinal averaged electron densities within 1.1 days. Additionally, the unbalance between the season and local time coverages of Swarm satellites during a 2 year period may also contribute to the differences between the two kinds of gradients.

#### 4.2. The F Region Electron Density During Daytime of EIA

The magnetic field at the equatorial region points nearly horizontally northward; therefore, the zonal electric field can cause the plasma to move vertically via  $E \times B$  drift. This vertical drift motion greatly affects the plasma density distribution in the ionospheric F region. As the plasma interacts with quite different neutral densities with changing altitudes, the recombination rate is strongly affected and the plasma composition changes [Kelley, 2009]. At the ionospheric F region the continuity equation for the electron or ion density,  $N$ , is defined as [Rishbeth, 2000; Prölss, 2004]

$$\frac{\partial N}{\partial t} = q - \beta \cdot N - \nabla(N \cdot v) \quad (3)$$

where  $q$  is the production rate,  $\beta$  is the linear loss coefficient, and  $v$  is the plasma drift velocity. The third term denotes the transport-induced effect, which shows the effect of drift on the electron density, depending on the velocity divergence and the movement of a preexisting gradient of electron density.

As seen in Figure 5c positive  $\Delta Ne$  is observed simultaneously shortly before 06:00 LT at both low and middle latitudes, implying that the F region electron density starts to increase due to the increased photoionization of the thermospheric gas after sunrise (the term  $q$  in equation (3)). This is most prominent for the equinoxes. For solstice months, the increase of electron density at middle latitudes appears earlier in the summer hemisphere due to the earlier Sun risetime in that hemisphere. Meanwhile, the equatorial zonal electric field also changes sign from westward to eastward around sunrise [Fejer *et al.*, 1991; Fejer *et al.*, 2008], causing the equatorial E and F region plasma to drift upward. At higher altitudes the downward diffusion of plasma along geomagnetic field lines becomes stronger, owing to the decrement of the collision between charged particles and neutral particles. Therefore, when the plasma transported to the height where the density gradient and gravity forces are strong enough, the downward diffusion of the plasma takes over the uplift process, and then the plasma mainly diffuses downward along the geomagnetic field lines into latitudes off the magnetic equator, forming two crest of EIA. The growth of the EIA starts, as seen from Figure 5c, around 07:00 LT and continues until 13:00 LT. A fast increase of electron density appears first at equatorial latitude between 07:00 and 10:00 LT, and the evolutions of the EIA crests generally follows the variations at the equator, but with 1–2 h delay depending on season (see Figure 6b). This implies that there is a 1–2 h delay between the eastward electric field uplifting of the plasma from the equatorial region, and subsequent diffusion downward, to the establishment of the EIA crests (back to Swarm altitude). A similar time scale of the EIA development has been reported by Stolle *et al.* [2008]. They found a typical response time of the EIA to variations in the zonal electric field of about 1–2 h. Once the EIA is well developed, the electron density at the trough region stays at rather stable level, mainly during equinox and December solstice, until presunset hours, while a slow decay of the EIA crests already starts in the afternoon.

The  $\Delta Ne$  development at the EIA crest regions is found also in good agreement with findings of Yeh *et al.* [2001]. The appearance of the crests at 09:00 LT, as deduced from their TEC tomography, is consistent with the start of increased  $\Delta Ne$  growth observed by Swarm. The subsequent poleward motion of the crests until 11:00 LT, reported by Yeh *et al.* [2001], is accompanied by an increasing local time gradient ( $\Delta Ne$ ), which implies an intensifying fountain effect that is reaching higher altitudes.

Another interesting feature of the EIA during daytime is the hemispheric asymmetry at solstice seasons. As shown in Figure 6b, the crest electron density is found to increase at almost the same rates in both hemispheres during equinox, while the crest in the summer hemisphere increases faster during solstice seasons from 06:00 LT to 10:00 LT. Before 10:00 LT, the plasma at the equator is mainly lifted up to higher altitudes via  $E \times B$  drift, and the downward diffusion of plasma along magnetic field lines from higher altitude to the

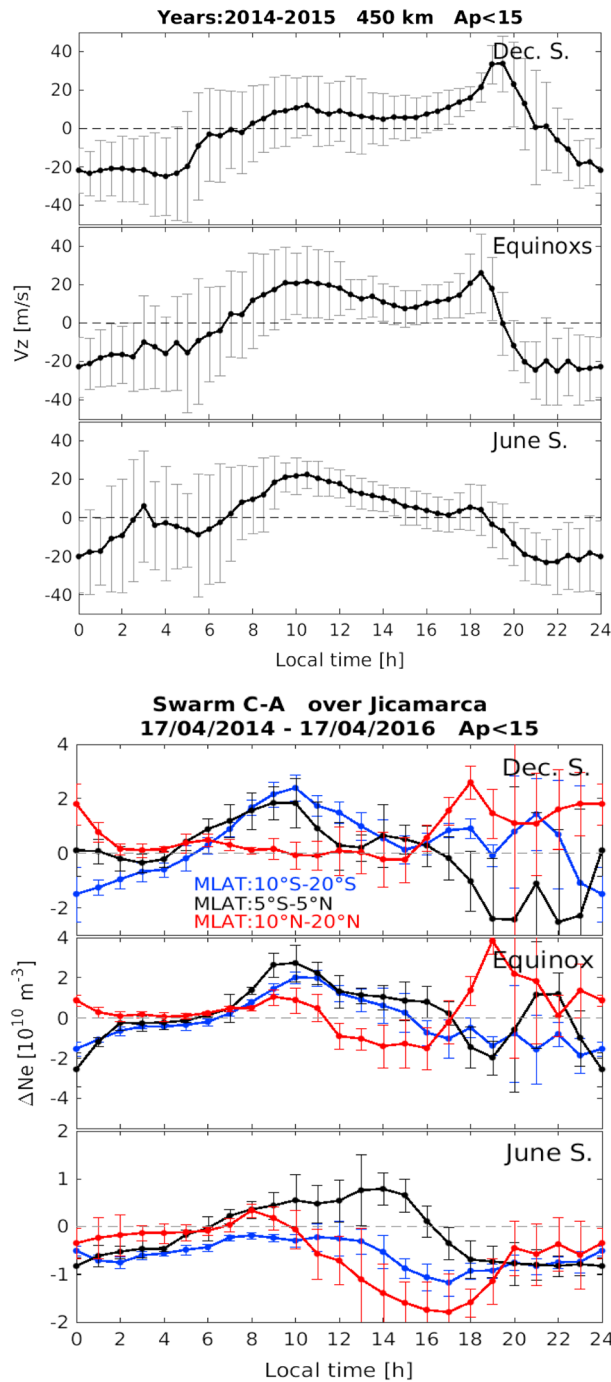


**Figure 7.** (a) The diurnal variations of the vertical plasma drift,  $v_z$ , measured by the incoherent scatter radar (ISR) at Jicamarca for three different seasons (positive values directing upward). The error bar indicates the standard deviation of  $v_z$ . (b) The diurnal variations of  $\Delta N_e$  derived by using the Swarm observations between  $\pm 15^\circ$  longitudes of Jicamarca radar. The error bars represent the uncertainty of mean value.

During all seasons  $v_z$  turns upward around 06:00 LT and reaches the maximum daytime value around 10:00 LT. Afterward, it decreases slightly to smaller amplitudes until presunset hours; meanwhile, the reduced photoionization during afternoon hours also partly contribute to the slight electron density decrement at afternoon as shown in Figure 5c. The vertical plasma drift starts to increase again around 17:00 LT

EIA crest regions may not be well established. Therefore, the production rate,  $q$ , in equation (3) takes the leading role for affecting the variations in the crest regions, which is larger in the summer hemisphere. The different offsets between the geographic and magnetic equators at different longitudes will also partly contribute to the longitudinal dependence of the ionospheric hemispheric asymmetry. Additionally, the transequator wind during solstice seasons will lift the  $F_2$  layer in the summer hemisphere to higher altitude, which may also contribute to the increase of topside electron density at a fixed altitude. When the EIA is well developed (after 10:00 LT), the transportation terms, including the fountain effect and the transequator wind-driven effect [Lin et al., 2007; Ram et al., 2009; Xiong et al., 2013], take over the role for controlling the variations of the crest electron density.

### 4.3. The Variations of F Region Electron Density Around Sunset and its Relation With the Vertical Plasma Drift

For comparison, Figure 7a presents the diurnal variations of the vertical plasma drift,  $v_z$ , measured by the Jicamarca ISR for different seasons (positive values representing upward velocity). For getting the diurnal variation of the vertical plasma drift, for each season we sorted the available radar observations into 1 h bins. The mean values are presented as black lines, and the error bar is the standard deviations for each local time. As the mean  $F_{10.7}$  during the considered 2 years is about 125 sfu, the seasonal and diurnal variations of  $v_z$  presented here are similar to those reported by Fejer et al. [1991] under moderate solar active condition ( $100 < F_{10.7} < 150$  sfu). During all

and peaks at 18:00–19:00 LT, in particular for December solstice and equinoxes. The sharp increase of the vertical drift corresponds to the PRE due to the enhanced eastward electric field in the ionospheric  $F$  region around sunset hours [e.g., Woodman, 1970; Fesen *et al.*, 2000].

The term  $q$  in equation (3) starts to decrease from afternoon to presunset and becomes negligible during dark hours. Suppose the loss coefficient,  $\beta$ , is constant during nighttime, the variation of the  $F$  region electron density is largely determined by the transportation term. As seen in Figures 5 and 6, a fast decrease of electron density is first seen at the trough region after 18:00 LT (relatively small for June solstice). However, a certain increase of electron density is found meanwhile at the EIA crest regions. The opposite variations of electron density at crest and trough regions around sunset can largely increase the crest-to-trough ratio (CTR) of EIA [e.g., Liu *et al.*, 2007; Xiong *et al.*, 2013]. And this evening variation is also different from the early developing process of the EIA (around 09:00 LT) when the  $F$  region electron density increases at both EIA trough and crest regions. A possible explanation is that during the EIA development phase in the morning, the plasma drifts are upward at both ionospheric  $E$  and  $F$  region. The process could be vividly described as there is continuous plasma lifted up from lower to higher altitudes. Besides, the enhanced ionization toward noon hours also partly contributes to the increase of  $F$  region electron density at both EIA trough and crest regions. However, after sunset the  $E$  region electron density decays fast, and the plasma lifted up partly evacuates the equatorial  $F$  region. Furthermore, the largely enhanced vertical drift during PRE forces the plasma to even higher altitudes. The results presented here imply that the PRE mainly affects the ionospheric  $F$  region.

As shown in Figure 7a, during December solstice and equinox, the vertical drift starts to decrease fast after 19:00 LT. The decrease or even reversed downward drift will stop lifting the plasma from the equatorial region. As a result the plasma diffusing from higher altitudes to the EIA crest regions is largely reduced. Additionally, the photoionization becomes negligible after sunset. Therefore, we see a decrease of electron density at crest regions after 19:00 LT. Interestingly, the minimum values of  $\Delta Ne$  at crest regions appear at 20:00 LT during equinox, which are 2 h earlier than that during December solstice. This difference can be well explained by the reverse time (from upward to downward) of the vertical plasma drift velocity, which appears at 19:00 LT during equinox and 2 h later for December solstice. Compared to the vertical plasma drift during PRE, we found a slight larger amplitude of  $v_z$  around 19:00 LT at December solstice than that at equinox, while the meanwhile electron density increase at EIA crest regions is more prominent at equinox season (see Figure 5c). One possible explanation could be that the vertical plasma drift has a prominent longitudinal dependence [Fejer *et al.*, 2008], while in this study we only used the drift data at Jicamarca longitude.

For better comparing with the vertical plasma drift measurements, Figure 7b presents that the diurnal variation of  $\Delta Ne$  only used the Swarm observations between  $\pm 15^\circ$  longitudes of Jicamarca radar. The diurnal variations of  $\Delta Ne$  are generally similar to the longitudinal averaged results as shown in Figure 6b, but with larger error bars (uncertainty of mean value) owing to the reduced number of observations. An interesting feature is that compared to the longitudinal averaged results,  $\Delta Ne$  at EIA crest regions is found to be with large hemispheric asymmetry at Jicamarca longitude (see the difference between the blue and red lines). A possible reason is that the transequator winds, which cause the hemispheric asymmetry of EIA, are also longitudinal dependent. Compared to the electron density at EIA crest regions, the  $Ne$  at EIA trough region seems to be more closely controlled by the vertical plasma drift.

#### 4.4. The Longitudinal Dependence of the $F$ Region Electron Density Local Time Gradient

As we know the ionospheric quantities at  $E$  and  $F$  region show prominent longitudinal wave patterns, due to tidal forcing from the lower atmosphere. To check whether the tidal forcing has similar effects on the electron density local time gradient between Swarm A and C, we considered a period centered on 15 August, when the well-known wave-4 is most prominent [Lühr *et al.*, 2012; Xiong and Lühr, 2013]. Observations within 133 days from Swarm A and C are needed for covering all the local times. Before presenting the local time gradient, we first show the local time versus longitude distributions of the normalized electron density ( $Ne$ ) in Figure 8a, separately for EIA crests (top and bottom) and equatorial (middle) regions. Clearly, wave-4 patterns during daytime are seen at the EIA crest regions, with wave maxima centered at  $-180^\circ\text{E}$ ,  $-90^\circ\text{E}$ ,  $0^\circ\text{E}$ , and  $90^\circ\text{E}$ , while the wave-4 pattern at the EIA trough region is not so clear. Comparing the two crest regions, we found the wave-4 patterns of  $Ne$  to be more prominent in the northern hemisphere. This hemispheric asymmetry may be caused by the chosen period, which overlaps to a good extent with the northern summer. Similarly, the local time versus longitude distributions of electron density local time gradient ( $\Delta Ne$ ) is presented in

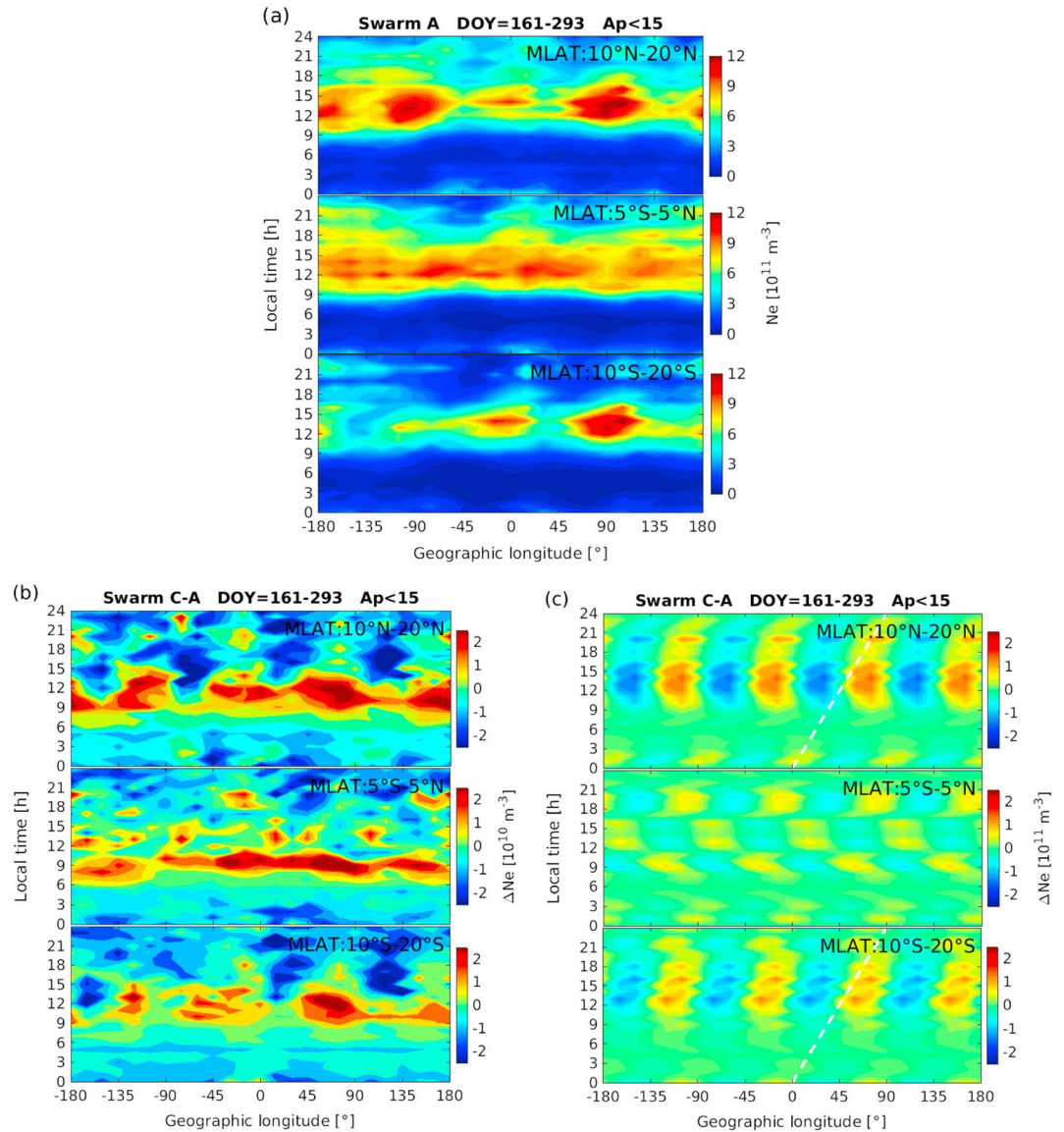


**Figure 8.** (a) The local time versus longitude variations of the electron density ( $Ne$ ) at EIA northern crest (top), equatorial (middle), and southern crest (bottom) regions during 133 days centered on the middle of August. (b) Similar as Figure 8 a but for the local time density gradient between Swarm C and A. (c) Similar as Figure 8b but for model fitted longitudinal wave-4 patterns, and the white dashed lines at EIA crest regions indicate the phase of tidal component DE3.

Figure 8b. The longitudinal wave-4 patterns are also found at the crest regions during 09:00–21:00 LT, while at the equatorial region the wave-4 pattern is not so clear. It just confined to the time around 09:00 LT. When compared with the wave-4 pattern of  $Ne$  at EIA crests, the wave-4 maxima of  $\Delta Ne$  of are found to be shifted eastward by about 22.5°.

For a better visualization of the tidal pattern we have applied a Fourier transform to the  $\Delta Ne$  data sampled along geographic longitude, separately for each local time hour. The resulting fourth harmonic signals at the three regions are presented in Figure 8c. In the two crest regions clear tidal signals appear over the time sector 09:00–21:00 LT. Before and after no coherent wave-4 pattern is obtained, especially for the southern hemisphere. The white dashed lines in Figure 8c (top and bottom) mark the tilt of a DE3 wavefront. The emerging wave patterns during 09:00–21:00 LT are reasonably well aligned with these guide lines and can therefore be related to the DE3 nonmigrating tidal component. Interestingly, no clear longitudinal wave pattern is found at the equatorial region.

**Table 1.** Amplitude and Phase of the Tidal Component DE3 in the Swarm Original Electron Density ( $N_e$ ) and in the Local Time Gradient ( $\Delta N_e$ ) Between Swarm A and C

|                | Swarm A                                |           | Swarm C-A                              |           |
|----------------|--|-----------|--|-----------|
|                | Amplitude ( $10^{10} \text{ m}^{-3}$ ) | Phase (h) | Amplitude ( $10^{10} \text{ m}^{-3}$ ) | Phase (h) |
| Northern crest | 11.2                                   | 14.5      | 0.87                                   | 20.7      |
| Southern crest | 11.3                                   | 14.1      | 0.97                                   | 20.0      |

In order to get more quantitative results on the tidal characteristics we fitted a DE3 signal to the wave-4 patterns shown in Figures 8a and 8b. For the analysis we considered only the data from the hours of clear tidal signals, 09:00–21:00 LT. The same tidal analysis is applied to both the original electron density measurements ( $N_e$ ) and the local time gradient ( $\Delta N_e$ ). In Table 1 the results are listed for the crest regions in the two hemispheres. Contrary to what is expected, the DE3 amplitude in  $\Delta N_e$  is slightly larger in the southern hemisphere. Obviously, other tidal components besides DE3, such as SPW4, SE2 and SW6, may also contribute to the wave-4 pattern in the north.

When comparing the results from the longitudinal differences with the original electron density data ( $N_e$ ), we see that the DE3 tidal amplitudes from  $\Delta N_e$  are 12.9 and 11.6 times smaller at the northern and southern crests, respectively, and the tidal phase (representing the DE3 crest passing the  $0^\circ$  longitude meridian) is delayed by 6.2 and 5.9 h from  $\Delta N_e$  at the two crest regions. A full discussion of the tidal features derived from the longitudinal gradient between Swarm A and C is beyond the scope of this study. More details of this topic can be found in our next study [Zhou *et al.*, 2016]. In that paper an expected amplitude ratio of 13.7 is quoted for DE3 and a phase delay of 6 h for the diurnal tides derived from the equatorial electrojet local time gradient,  $\Delta E E J$ . The values we obtained are in reasonable agreement with the theoretical prediction. This confirms that the  $\Delta N_e$  between Swarm A and C can be used for looking at the tidal activity from a different perspective.

The strong control of the  $F$  region electron density by the  $E$  region dynamo during daytime is also evident from the longitudinal wave patterns presented in Figure 8. During the developing phase of the EIA (hours 09:00–12:00 LT), the maxima of wave-4 patterns appear at about the same longitudes for EIA trough and crest regions. Compared to wave minima longitudes the enhanced  $E \times B$  drift at wave maxima longitudes lifts the plasma to higher altitude and makes the electron density at these longitudes increases faster. Additionally, the longer diffusion path length also makes the plasma at wave maxima longitudes needs longer time before it diffuses down to Swarm altitude. When the EIA stops to develop at afternoon hours, the relatively larger  $E \times B$  drift at wave maxima longitudes and the larger diffusing time make the electron density decreases slower at these longitudes when compared to that at wave minima longitudes (see the blue areas at EIA crest regions during 13:00–21:00 LT in Figure 8b).

## 5. Summary

In this study we present the diurnal evolution of  $F$  region electron density at low and middle latitudes by using observations from the Swarm constellation. The local time gradients derived from single satellite (Swarm A) as well as from the two side-by-side flying satellites (Swarm A and C) have been compared, and we consider that the electron density local time gradient derived from the twin satellites is more reasonable. The main findings can be summarized as follows:

1. The electron density increase starts just at sunrise (around 06:00 LT) simultaneously at low and middle latitudes due to the increased photoionization. At equatorial latitudes the increase in electron density gets even steeper after 07:00 LT, and the steepest increase of electron density (about  $3 \cdot 10^{10} \text{ m}^{-3}$  within 6 min) occurs around 09:00 LT. We suggest the upward vertical plasma drift in connection with the buildup of the equatorial fountain effect to play a major role.
2. The local time variation of the EIA crest electron density during daytime is similar to the respective evolutions at the equator, but with 1–2 h delayed. We relate this delay to the response time between the equatorial electric field and the buildup of the plasma fountain.
3. At equinox months a fast decrease of the  $F$  region electron density is seen at the EIA trough region during PRE, while an increase is found meanwhile at crest regions. The antiphase variations of the electron

density at the EIA crest and trough regions are caused by the enhanced vertical plasma drift during PRE. Afterward, a fast decrease of the EIA crest electron density occurs between 19:00 and 23:00 LT, with seasonal dependence.

- The electron density local time gradient between Swarm A and C also shows clear longitudinal wave patterns around months of August, particularly prominent during daytime is the wave-4 pattern, which we attributed to the tidal forcing from the lower atmosphere. It confirms the close control of the daytime  $F$  region electron density by the  $E$  region dynamo via the vertical  $E \times B$  plasma drift. We suggest that the higher uplift of the plasma at the longitudinal wave maxima will reduce the decay of the EIA crest electron density during afternoon hours than that at the wave minima longitudes. An interpretation of the tidal features in the electron density local time gradient between Swarm A and C can provide additional information on the tidal modes in the ionosphere.

#### Acknowledgments

The authors want to thank Claudia Stolle for the fruitful discussion. The European Space Agency is acknowledged for providing the Swarm data. The official Swarm website is <http://earth.esa.int/swarm>, and the server for Swarm data distribution is <ftp://swarm-diss.esa.int>. The vertical drift data from the incoherent scatter radar at Jicamarca can be downloaded from the Madrigal database at Haystack observatory (<http://madrigal.haystack.mit.edu/madrigal/>). Chao Xiong is partly supported by National Nature Science Foundation of China (grant 41431073). Yun-Liang Zhou is supported by China Scholarship Council and National Nature Science Foundation of China (41274194).

#### Reference

- Abdu, M. A., G. O. Walker, B. M. Reddy, J. H. A. Sobral, B. G. Fejer, T. Kikuchi, N. B. Trivedi, and E. P. Szuszczewicz (1990), Electric field versus neutral wind control of the equatorial anomaly under quiet and disturbed condition: A global perspective from SUNDIAL 86, *Ann. Geophys.*, *8*, 419–430.
- Appleton, E. V. (1946), Two anomalies in the ionosphere, *Nature*, *57*, 691, doi:10.1038/157691a0.
- Aydogdu, M. (1988), North-south asymmetry in the ionospheric equatorial anomaly in the African and the West Asian regions produced by asymmetrical thermospheric winds, *J. Atmos. Terr. Phys.*, *50*, 623–627, doi:10.1016/0021-9169(88)90060-8.
- Beylkin, G., R. Coifman, and V. Rokhlin (1991), Fast wavelet transforms and numerical algorithms, *Commun. Pure Appl. Math.*, *44*, 141–183, doi:10.1002/cpa.3160440202.
- Chapman, S., and R. S. Lindzen (1970), *Atmospheric Tides: Thermal and Gravitational*, Gordon and Breach, New York.
- Duncan, R. A. (1959), The equatorial F-region of the ionosphere, *J. Atmos. Terr. Phys.*, *18*, 89–100, doi:10.1016/0021-9169(60)90081-7.
- Eccles, J. V., J. P. S. Maurice, and R. W. Schunk (2015), Mechanisms underlying the prereversal enhancement of the vertical plasma drift in the low-latitude ionosphere, *J. Geophys. Res. Space Physics*, *120*, 4950–4970, doi:10.1002/2014JA020664.
- Fejer, B. G., E. R. dePaula, S. A. González, and R. F. Woodman (1991), Average vertical and zonal F region plasma drifts over Jicamarca, *J. Geophys. Res.*, *96*(A8), 13,901–13,906, doi:10.1029/91JA01171.
- Fejer, B. G., J. W. Jensen, and S.-Y. Su (2008), Quiet time equatorial F region vertical plasma drift model derived from ROCSAT-1 observations, *J. Geophys. Res.*, *113*, A05304, doi:10.1029/2007JA012801.
- Fesen, C., G. Crowley, R. G. Roble, A. D. Richmond, and B. G. Fejer (2000), Simulation of the pre-reversal enhancement in the low latitude vertical ion drifts, *Geophys. Res. Lett.*, *27*, 1851–1854, doi:10.1029/2000GL000061.
- Heelis, R. A. (2004), Electrodynamics in the low and middle latitude ionosphere: A tutorial, *J. Atmos. Sol.-Terr. Phys.*, *66*, 825–838, doi:10.1016/j.jastp.2004.01.034.
- Huang, Y.-N., K. Cheng, and S.-W. Chen (1989), On the equatorial anomaly of the ionospheric total electron content near the Northern Anomaly Crest Region, *J. Geophys. Res.*, *94*, 13,515–13,525, doi:10.1029/JA094iA10p13515.
- Immel, T. J., E. Sagawa, S. L. England, S. B. Henderson, M. E. Hagan, S. B. Mende, H. U. Frey, C. M. Swenson, and L. J. Paxton (2006), Control of equatorial ionospheric morphology by atmospheric tides, *Geophys. Res. Lett.*, *33*, L15108, doi:10.1029/2006GL026161.
- Kelley, M. C. (2009), *The Earth's Ionosphere: Electrodynamics and Plasma Physics*, 2nd ed., Elsevier, New York.
- Kudeki, E., S. Bhattacharyya, and R. F. Woodman (1999), A new approach in incoherent scatter F region  $E \times B$  drift measurements at Jicamarca, *J. Geophys. Res.*, *104*(A12), 28,145–28,162, doi:10.1029/1998JA900110.
- Liang, P. H. (1947), F2 ionization and geomagnetic latitudes, *Nature*, *160*(11), 642–643, doi:10.1038/160642a0.
- Lin, C. H., J. Y. Liu, T. W. Fang, P. Y. Chang, H. F. Tsai, C. H. Chen, and C. C. Hsiao (2007), Motions of the equatorial ionization anomaly crests imaged by FORMOSAT-3/COSMIC, *Geophys. Res. Lett.*, *34*, L19101, doi:10.1029/2007GL030741.
- Liu, H., C. Stolle, M. Förster, and S. Watanabe (2007), Solar activity dependence of the electron density in the equatorial anomaly regions observed by CHAMP, *J. Geophys. Res.*, *112*, A11311, doi:10.1029/2007JA012616.
- Liu, L., M. He, W. Wan, and M.-L. Zhang (2008), Topside ionospheric scale heights retrieved from Constellation Observing System for Meteorology, Ionosphere, and Climate radio occultation measurements, *J. Geophys. Res.*, *113*, A10304, doi:10.1029/2008JA013490.
- Lühr, H., M. Rother, K. Häusler, B. Fejer, and P. Alken (2012), Direct comparison of non-migrating tidal signatures in the electrojet, vertical plasma drift and equatorial ionization anomaly, *J. Atmos. Sol. Terr. Phys.*, *75–76*, 31–43, doi:10.1016/j.jastp.2011.07.009.
- Namba, S., and K. I. Maeda (1939), *Radio Wave Propagation*, pp. 86, Corona, Tokyo.
- Pröls, G. W. (2004), *Physics of the Earth's Space Environment*, Springer, Berlin.
- Ram, S. T., S. Y. Su, and C. H. Liu (2009), FORMOSAT-3/COSMIC observations of seasonal and longitudinal variations of equatorial ionization anomaly and its inter-hemispheric asymmetry during the solar minimum period, *J. Geophys. Res.*, *114*, A06311, doi:10.1029/2008JA013880.
- Rishbeth, H. (1971a), The F-layer dynamo, *Planet. Space Sci.*, *19*, 263–267, doi:10.1016/0032-0633(71)90205-4.
- Rishbeth, H. (1971b), Polarization fields produced by winds in the equatorial F-region, *Planet. Space Sci.*, *19*, 357–369, doi:10.1016/0032-0633(71)90098-5.
- Rishbeth, H. (2000), The equatorial F-layer: Progress and puzzles, *Ann. Geophys.*, *18*, 730, doi:10.1007/s00585-000-0730-6.
- Sagawa, E., T. J. Immel, H. U. Frey, and S. B. Mende (2005), Longitudinal structure of the equatorial anomaly in the nighttime ionosphere observed by IMAGE/FUV, *J. Geophys. Res.*, *110*, A11302, doi:10.1029/2004JA010848.
- Stolle, C., C. Manoj, H. Lühr, S. Maus, and P. Alken (2008), Estimating the daytime Equatorial Ionization Anomaly strength from electric field proxies, *J. Geophys. Res.*, *113*, A09310, doi:10.1029/2007JA012781.
- Woodman, R. F. (1970), Vertical drift velocities and east-west electric fields at the magnetic equator, *J. Geophys. Res.*, *75*(31), 6249–6259, doi:10.1029/JA075i031p06249.
- Xiong, C., and H. Lühr (2013), Nonmigrating tidal signatures in the magnitude and the inter-hemispheric asymmetry of the equatorial ionization anomaly, *Ann. Geophys.*, *31*, 1115–1130, doi:10.5194/angeo-31-1115-2013.
- Xiong, C., H. Lühr, and S. Y. Ma (2013), The magnitude and inter-hemispheric asymmetry of equatorial ionization anomaly-based on CHAMP and GRACE observations, *J. Atmos. Terr. Phys.*, *105*, 160–169, doi:10.1016/j.jastp.2013.09.010.

- Xiong, C., C. Stolle, H. Lühr, J. Park, B. G. Fejer, and G. N. Kervalishvili (2016), Scale analysis of the equatorial plasma irregularities derived from Swarm constellation, *Earth Planets Space*, *68*, 121, doi:10.1186/s40623-016-0502-5.
- Yeh, K. C., S. J. Franke, E. S. Andreeva, and V. E. Kunitsyn (2001), An investigation of motions of the equatorial anomaly crest, *Geophys. Res. Lett.*, *28*(24), 4517–4520, doi:10.1029/2001GL013897.
- Zhou, Y. L., H. Lühr, P. Alken, and C. Xiong (2016), New perspectives on equatorial electrojet tidal characteristics derived from the Swarm constellation, *J. Geophys. Res. Space Physics*, *121*, 7226–7237, doi:10.1002/2016JA022713.